

# ASSESSMENT OF ORBIT DETERMINATION ACCURACY OF RADAR NETWORKS

Martin Käske<sup>(1)</sup>, Marcus Albrecht<sup>(1)</sup>, Isabel Schlangen<sup>(2)</sup>, and Hans Schily<sup>(2)</sup>

<sup>(1)</sup>Fraunhofer Institute for High Frequency Physics and Radar Techniques FHR, Fraunhoferstr. 20, 53343 Wachtberg, Germany, Email: {martin.kaeske, marcus.albrecht}@fhr.fraunhofer.de

<sup>(2)</sup>Fraunhofer Institute of Communications, Information Processing and Ergonomics FKIE, Fraunhoferstr. 20, 53343 Wachtberg, Germany, Email: {isabel.schlengen,hans.schily}@fkie.fraunhofer.de

## ABSTRACT

Multistatic radar networks are a promising concept to accurately determine the orbital parameters of objects in space. The assessment of their performance, especially in an analytical manner, poses a challenge, due to the numerous degrees of freedom in designing a network layout. This paper uses a simulation based approach, to assess a network with two nodes where the distance between them and their geographical arrangement are varied. The ability to determine orbital parameters are computed for a set of different orbits. For each one of them estimated radar observations are generated using a stochastic model. The parameter estimation is modeled as either grid based (i.e. using range, Doppler, etc. cells) or grid free (e.g. using nonlinear gradient based estimators). The orbit determination is characterized using lower bounds of a tracking based method. A goal of the paper is to find a single best distance between nodes, leading to the least possible error. However, this proved to not exist, at least not for a wide range of different orbits.

Keywords: Space Surveillance; Multistatic Radar Networks; Simulation; Radar Signal Processing; Orbit Determination.

## 1. INTRODUCTION

With the increasing amount of active and inactive satellites in orbit, their accurate observation becomes more and more important to avoid fatal collisions in space. Observations of objects in space are typically performed using optical instruments (see [1, 2] as examples) or radar. Radar has the inherent benefit of being independent on weather conditions and the ability to determine the range of an object (which require laser ranging for optical observations). For radar measurement, the use of large monostatic systems is a well tested approach. The radars can consist of powerful single dish antennas, such as the TIRA [3] system or comprised of a phased array such as GESTRA [4, 5]. In both cases objects are detected and tracked over time in order to gather enough information

to reliably determine their orbits. Multistatic radars [6] offer, in general, the additional benefit of improved coverage and exploitation of varying aspect angles and the bistatic radar cross section (RCS) of a target. The use of radar networks takes this a step further by combining mono- and multistatic systems and jointly process the obtained observations. One can interpret networks as using multiple observations from different locations in space to determine an orbit as opposed to the using multiple observations over time. Examples for networks for space surveillance applications are EISCAT (European Incoherent Scatter Scientific Association) [7] and GRAVES (Grand Réseau Adapté à la Veille Spatiale) [8].

The use of a radar network makes the assessment of the performance of the determination of orbit parameters more complicated as it introduces new degrees of freedom. The number of nodes in the network, their relative position to each other, the orientation of the field of view (FoV) of the transmitter and in general the type of nodes (either transmitter, receiver or transceiver) will most likely impact the performance. Since it is not feasible to analytically or theoretically investigate the radar network a simulative approach is used instead. In this paper the work of [9] is extended, by investigating the performance of a two node network, with varying baselines and two different orientations (north-south or east-west). The trajectories of objects in different orbits were simulated over a duration of four weeks. For a simulated FoV of a transmitter, observations of the network nodes are derived using a stochastic model of the signal processing framework. Finally, orbital parameters are assumed to be determined using a tracking based approach with respective performance bounds being used to measure the accuracy of the orbit determination. Furthermore, the orientation of the FoV is set to be either along or across the line connecting the two nodes. Two different signal processing strategies are considered. For the grid based method the accuracy of the simulated observations is mainly limited by the chosen grid size, where the grid free case simulates an estimation procedure that reaches the Cramer-Rao lower bound (CRLB). The obtained results show, as expected, a much better performance in terms of location and velocity error in the grid free case. Another aim of the paper is to investigate the existence of a best distance between the nodes, which leads to the smallest

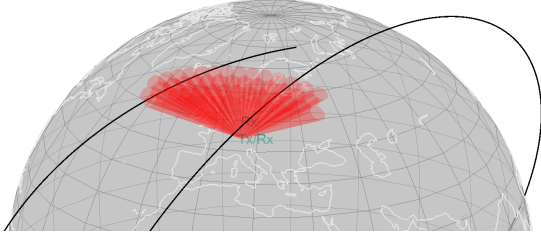


Figure 1: Exemplary setup with a vertical network, a horizontal FoV and a single object in orbit

possible error. However, this much can be anticipated, such a baseline apparently does not exist, at least not for all possible orbits.

## 2. SIMULATION APPROACH

### 2.1. Radar Network Setup

The simulations performed for this work are based on the ones conducted in [9]. The general setup is to have two nodes in a network, where one is equipped with both a transmitter and a receiver while the second node is a receiver only. The two nodes are separated either in a north-south or east-west manner with some length of the baseline. The former is referred to as *vertical network* or *V-Net* and the latter *horizontal network* or *H-Net*. In total 20 baselines are considered in the range  $[1, 50, 100, \dots, 950]$  km. The midpoint or center of the baseline is fixed in each case at  $N50^{\circ}30' E10^{\circ}0'$ , denoting some arbitrary location in central Germany. The position of the transmitter and receiver nodes respectively is given by half the baseline relative to the center of the network. This means, with increasing baseline the location of both nodes is changing along the predetermined direction.

The radar system assumed in this work is equipped with phased arrays on each node and is working in a search mode. This means the goal is to monitor a rather extended region of space instead of, for example, following the trajectory of a specific object. A major benefit of a phased array system, is the possibility to form and steer transmit or receive antenna beams free of inertia in very rapid succession. In a pulsed radar, where multiple pulses are aggregated to form a coherent processing interval (CPI), it is therefore possible to quickly and repeatedly scan a certain (angular) region by placing beams at different (angular) positions for each CPI. A predefined FoV is therefore determined as a collection of beam positions that are periodically addressed. The term *search fence* is sometimes used to emphasize that the FoV is covered by a number of beams instead of being observed at once.

For the work presented in this paper the FoV is defined from the point of view of the transmitter, with both receivers being assumed to adjust their beams in a way that

$a - r_E$	$[300, 400, 500, \dots, 1600]$ km
$i$	$[45, 47, 49, \dots, 89]^{\circ}$
$\Omega$	$307.1577^{\circ}$
$\omega$	$91.5062^{\circ}$
$e$	0.000 235 2
$\nu$	0

Table 1: Classical orbital elements of the simulated objects

the volume illuminated by a transmit beam is fully covered. Due to the multistatic nature of the network this implies that the remote receiver (i.e. second node in the network) may need to use more than one beam to cover a specific transmit beam. To not further introduce additional degrees of freedom in the simulation, the FoV is always centered towards the local zenith, i.e. upwards, right above the transmitter. The FoV has a fixed angular extent of  $90^{\circ} \times 15^{\circ}$  with two distinct orientations *horizontal* and *vertical* respectively. In the results sections the terms *H-FoV* and *V-FoV* will be used to distinguish. The orientations follow the definitions of the extent of the networks. When the longer angular extent of the FoV is orientated along the baseline of a horizontal network it will be referred to as *horizontal FoV*. In the opposite case, of the longer extent being along the vertical baseline, the term *vertical baseline* will be used. Four different combinations can therefore be identified, where for each type of network, the FoV can be either aligned along the baseline or perpendicular to it. An example is illustrated in Figure 1 showing a network being extended along the vertical axis (transceiver (Tx/Rx) and second receiver (Rx) are separated in north-south direction). The FoV is horizontally oriented in this case with the individual transmit beams that make up the search fence being shown as individual cones. In addition a single orbit is illustrated over roughly one and a half orbital periods, to illustrate how it eventually enters the FoV.

### 2.2. Generation of Observations

With the network layout and FoV setup the different orbits or rather objects in orbit can be simulated. The trajectories of a number of objects will be simulated over a duration of four weeks. For each object it will be determined if and when it enters the FoV and what parameters a hypothetical signal processing framework in the receivers would return. Orbits are generated as Keplerian orbits [10, Chapter 2] based on a regular grid in inclination ( $i$ ) and semimajor axis ( $a$ ) of the classical orbital elements [10, Section 2.4.1] associated with them. From the Table 1 it can be seen that the remaining orbital elements are fixed to rather arbitrary values. Since each object is observed over a rather long time span (four weeks), it can be expected that regardless of the true anomaly  $\nu$ , argument of perigee  $\omega$  and longitude of the ascending node  $\Omega$  the object will eventually pass through the search fence. Therefore, their concrete values (in conjunction with a fixed eccentricity  $e$ ) should not influence the investiga-

RCS	5 m <sup>2</sup>
average power	20 kW
dwelt time $t_{dwell}$	0.2 s
wavelength $\lambda$	0.2 m
bandwidth $B$	1 MHz
3 dB beamwidth $\Omega_{3dB}$	0.105 rad

Table 2: Radar and target parameters

tions conducted for this paper. The inclination  $i$  on the other hand determines more or less directly if an orbit ever crosses the FoV and under which angle. The semimajor axis  $a$  is largely influencing the achievable signal to noise ratio (SNR) in both a mono- and bistatic configuration. It should be noted that Table 1 shows  $a - r_E$  instead of the semimajor axis  $a$ . This is the difference between the semimajor axis and the average earth radius and is done primarily to present the values in a more intuitive manner as an approximate measure of the height of an object above ground.

The transmitter of the radar network is assumed to be in constant search mode continuously cycling through the different beam positions of the search fence with a fixed *dwelt time* of each beam. For each of the 322 orbits/objects it is determined when, if at all, they are entering an active beam (i.e. a beam is active when it is its turn in the search fence). The dwelt time is set to be  $t_{dwell} = 0.2$  s and denotes to largest time span an individual object is observed in a given beam. It is possible that the observation time is shorter than the dwelt time, when either an object has a high (angular) velocity or is passing through a small segment of the area covered by a beam. It is furthermore possible that an object is observed multiple times during an orbital period (or overflight) if it moves slow enough to be captured during multiple cycles of the search fence. This is more likely to happen for orbits with higher altitudes as they tend to have smaller angular velocities.

Based on the possible detections (i.e. when an object crosses a beam) actual detections are determined using their probability of detection ( $P_D$ ). The  $P_D$  is determined according to the equations given in [11, Table 15-2] for a *Swerling 0* target using a square law detector. As a prerequisite, the SNR needs to be computed which is done as defined in [11, Section 2.10] under the assumption of coherent integration during the observation time. The required parameters of the radar as well as the assumed RCS of the target are listed in Table 2.

After a detection is confirmed by its  $P_D$ , observation parameters are generated. They represent the parameters an actual radar signal processing framework would obtain and encompass distance to the node  $r$  (range), radial velocity  $v_r$  and direction of arrival  $\Omega$  (denoted as *uv* or *direction cosine* components). The basis of the observation is always the ground truth as determined by the simulated orbital trajectory and projection to the respective receiver location. Any actual radar would however be influenced by unavoidable measurement noise and potential limita-

tions of the signal processing algorithm used. In order to reflect this, artificial noise is added to the ground truth values. Each observed parameter follows a normal distribution with the ground truth as its mean.

$$\begin{aligned}\hat{r} &\propto \mathcal{N}\left(r_0, \sigma_{r_n}^2 + \sigma_{r_p}^2\right) \\ \hat{v} &\propto \mathcal{N}\left(v_0, \sigma_{v_n}^2 + \sigma_{v_p}^2\right) \\ \hat{\Omega}_u &\propto \mathcal{N}\left(\Omega_{u_0}, \sigma_{\Omega_n}^2 + \sigma_{\Omega_p}^2\right) \\ \hat{\Omega}_v &\propto \mathcal{N}\left(\Omega_{v_0}, \sigma_{\Omega_n}^2 + \sigma_{\Omega_p}^2\right)\end{aligned}\quad (1)$$

Please note, that in practice a radar would determine the multistatic range (sum of distances to transmitter and receiver) but in the simulation the monostatic one is used. By design there is always at least one monostatic configuration for each transmitter in the network, allowing to estimate the distance of the object to the transmitter and subsequently the one-way range to any receiver. The variance of the distribution is generally determined by two terms.

$$\sigma^2 = \sigma_n^2 + \sigma_p^2 \quad (2)$$

The first term,  $\sigma_n^2$ , denotes the inherent random deviation of an estimated value from its true value caused by measurement noise. If an estimator uses the maximum likelihood principle (and is unbiased) this type of variance is ultimately lower bounded by the CRLB [12]. For the investigations done in this paper the approximations for the CRLB as defined in [13] are used. The variance  $\sigma_n^2$  depends on the concrete SNR as it is caused by measurement noise. The second term,  $\sigma_p^2$ , on the other hand is independent of the SNR and denotes deviations caused by the signal processing algorithm. If a parameter estimation algorithm uses a grid-based search, its accuracy is ultimately limited by the size of the grid. In radar signal processing the range- and doppler-cell size can define such grid sizes. Both are actually resolution limits as they denote the limit where it is not possible anymore for an algorithm to decide if one or more targets are simultaneously present. Such limits typically do not consider the possibility of using super-resolution or multi-target parameter estimation methods to further increase the resolution limit. If the granularity of a search grid is set to be  $\Delta$ , the largest possible error caused by the grid is  $\Delta/2$ . This is similar to the quantization of an analog signal and the standard deviation of the error, assuming the true value is sufficiently randomly distributed, can be approximated as follows [11, Section 14.3].

$$\sigma_p^2 = \frac{\Delta^2}{12} \quad (3)$$

For the simulations at hand the following values for the deviation caused by the signal processing are used.

$$\begin{aligned}\sigma_{r_p} &= \frac{0.886c_0}{2B\sqrt{12}} = 38.8 \text{ m} \\ \sigma_{v_p} &= \frac{\lambda}{2t_{dwell}\sqrt{12}} = 0.144 \text{ m s}^{-1} \\ \sigma_{\Omega_p} &= \frac{\Omega_{3dB}}{10} = 0.0105 \text{ rad}\end{aligned}\quad (4)$$

With  $c_0$  being the speed of light. The values for range and radial velocity are closely related to typical cell sizes.  $\sigma_{\Omega_p}$  on the other hand is a coarser approximation as it relates the accuracy of the direction of arrival to the beamwidth of the transmit beam. It must be stressed again that all variants of  $\sigma_p$  are determined by the signal processing algorithm chosen and are thus, to some extent, adjustable by the operator. The deviations caused by the measurement noise,  $\sigma_n^2$ , on the other hand are inherent limits of the data itself. Depending on the SNR of a detection one of the two terms dominates the overall accuracy of the parameters. At a rather low threshold of the SNR, the accuracy cannot be further increased when a grid-based method is used. As an example, for the simulations setup used here, at a SNR > 6 dB the total variance is dominated by the grid part (i.e.  $\sigma_{r_p} > \sigma_{r_n}$ ). Due to the RCS and the upper bound on the orbit height of the target, the resulting SNR normally well exceeds this limit. Therefore, results will be shown later on where the accuracy is only limited by the CRLB denoting a situation where a grid-free (superresolution) technique is assumed yielding the theoretical best accuracy achievable.

### 2.3. Determination of Orbit Accuracy

With the detections and their associated observation parameters the orbits can be determined. The location and velocity (in Cartesian space) will be used as state vectors instead of the orbital elements. The procedure applied is the same as has been used in [9] and details can be found there. In short, for each overflight of an object/orbit all possible observations are gathered and used as an input for a Kalman filter based tracker. The filter is adapted to predict targets following a Keplerian motion. The procedure is sequentially repeated for the whole simulation duration of four weeks. In order to evaluate the accuracy of the tracking process the posterior Cramer-Rao lower bound (PCRLB) [14] is employed. For each overflight the PCRLB is computed and serves as an (optimistic) estimate of the state covariance matrix. The computation of the PCRLB require a current state and state covariance matrix as input. Since there is typically a long time span between subsequent overflights, the next state covariance matrix cannot be easily predicted from a previous one due to the Keplerian motion. Therefore, an experimental approach is used [9] for the prediction where the covariance matrix is estimated using a Monte-Carlo approach.

The PCRLB or rather the state covariance matrix of the last usable overflight will be used to ultimately determine the accuracy with which an orbit can be estimated. The covariance matrix has six dimensions denoting three coordinates in Cartesian space in conjunction with three velocity components. When the covariance matrix is interpreted as a six dimensional error ellipsoid, its determinant can be used as a measure of its volume and can be used to compare different matrices.

$$V = \sqrt{\det(\Sigma_{\hat{\theta}\hat{\theta}})} \quad (5)$$

With  $\hat{\theta} = [\hat{x}, \hat{y}, \hat{z}, \hat{v}_x, \hat{v}_y, \hat{v}_z]$  being the six dimensional state vector and  $\Sigma_{\hat{\theta}\hat{\theta}}$  the associated covariance matrix.

The volume of a six dimensional ellipsoid can be difficult to interpret, which is why in this work, as opposed to [9], the covariance matrix is split into a location and velocity matrix.

$$\Sigma_{\hat{\theta}\hat{\theta}} = \begin{bmatrix} \Sigma_{\hat{\theta}_r, \hat{\theta}_r} & \cdots \\ \cdots & \Sigma_{\hat{\theta}_v, \hat{\theta}_v} \end{bmatrix} \quad (6)$$

For both submatrices the determinant and therefore a sub-error-volume is computed.

$$V_r = \sqrt{\det(\Sigma_{\hat{\theta}_r, \hat{\theta}_r}), V_v = \sqrt{\det(\Sigma_{\hat{\theta}_v, \hat{\theta}_v})} \quad (7)$$

The relation  $V = V_r \cdot V_v$  only holds if the location and velocity terms are uncorrelated (i.e.  $\Sigma_{\hat{\theta}_r, \hat{\theta}_v} = \mathbf{0}$ ) which is an assumption made for this investigation.

## 3. RESULTS

In this section the results for the location and velocity error volume are presented for different orbits and network configurations. The values of the error volumes will be shown in logarithmic scale, using the decadic logarithm ( $\log_{10}(V)$ ). This is necessary since the obtained values can vary over multiple orders of magnitude, which is difficult to represent in linear scale. An intuition for the meaning of the error volume can be the edge length of an equivalent cube instead of an ellipsoid. It can be computed as  $\sqrt[3]{V}$  such that a value of e.g.  $\log_{10}(V_r) = 9$  is equivalent to an error cube with 1 km edge length. It must be noted that the error volume or equivalent cube length says nothing about the distribution of the error in the three coordinate axes. This means an error volume can be large if the location error is large only along the trajectory but not across it. Consider as an example the angular limits of (4). If the accuracy of the angular estimates is 0.0105 rad in both u- and v-coordinates, the error area spanned at a distance of 500 km is  $(\sin(0.0105) \cdot 500 \text{ km})^2 \approx (5250 \text{ m})^2$ . Together with the range accuracy of 38.8 m this yields an equivalent cube length of  $\sqrt[3]{(5250 \text{ m})^2 \cdot 38.8 \text{ m}} \approx 1 \text{ km}$ . This seemingly large error is, however, mainly due to the inaccuracy in the angular estimates of the simulated signal processing scheme. In case a specific orbit cannot be observed by the network, for example if the object never enters the FoV or an insufficient number of detections is provided to the orbit determination algorithm, a blank value will be shown in the plots (white background).

For all the results it must be borne in mind that the simulations contain many variables that can lead to a specific error volume. In general one would expect that the higher the SNR the better the results. However, due to the effects of a grid based signal processing this might not be reflected in the results. Furthermore, the errors are lower the more detections or the more overflights are passed to

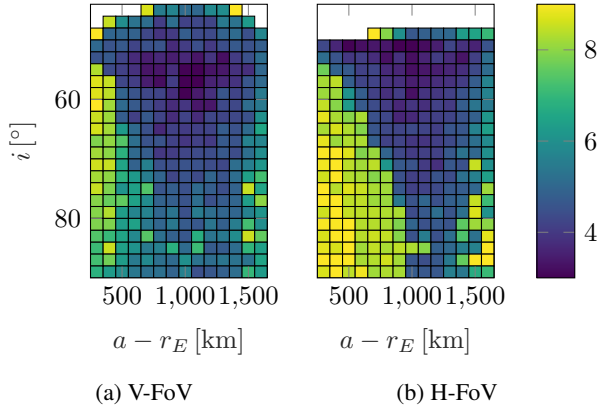


Figure 2: H-Net 1 km baseline error location Grid

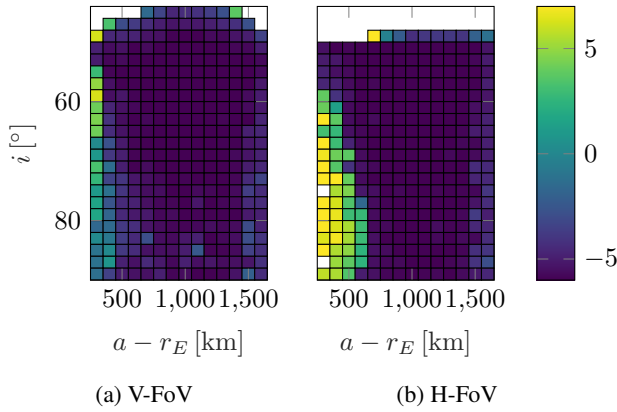


Figure 3: H-Net 1 km baseline error velocity Grid

the orbit determination and tracking framework. The geometrical constellation on the other hand, either due to the network layout, FoV orientation or orbital parameters might counteract leading to an unexpected decrease of accuracy. Therefore, it will in general not be possible to name a single cause for a specific behavior of the errors volumes shown in the following sections.

### 3.1. Results 1km Baseline Error

For the first example the second receiver is only 1 km away from the transceiver node. In essence, this creates a second monostatic configuration. The extent of the network in either horizontal or vertical direction makes no difference, which is why results are only shown for the horizontal case. There is, however, a dependency on the orientation of the FoV. Figure 2 shows the results for the error in terms of location, while Figure 3 shows the results for the velocity.

It can be seen that in general the error is larger for lower orbits and higher inclinations. Although a lower orbit should exhibit increased SNR the effect appears to be counteracted by a shorter time an object spends in the FoV during one overflight. The effect is more pronounced for the horizontal FoV shown in Figure 2b. It

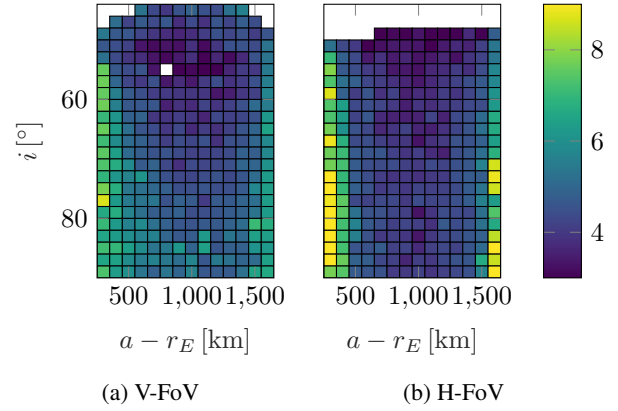


Figure 4: V-Net 500 km baseline error location Grid

could be speculated that this is due to, in general, unfavorable geometric constellations as the object passes through the FoV across the longer extent. This means that the object may stay longer in the vertical FoV when passing through in north south direction and thus generating more observations. An effect that will be seen also later on is that the smallest error volumes (for location and to lesser extent velocity) can be seen for mid-range orbits at an inclination of around  $50^\circ$ . Whether this just happens to coincide with the latitude of the center of the network (N $50^\circ 30'$ ) has yet to be investigated.

### 3.2. Results 500km Baseline Error

For the second example the distance between the transceiver and the second receiver is increased to 500 km. Since the second receiver now forms a proper bistatic configuration with the transmitter the results are shown for both the vertical and horizontal network. Figure 4 depicts results for the location error of the vertical and Figure 5 of the horizontal network respectively. The effect of larger location errors at low orbits is less strong but still noticeable, especially for the horizontal network with horizontal FoV. The *valley of low error* at mid-range heights and inclinations around  $50^\circ$  is yet again noticeable. Overall, it can be concluded that the error in location is lowered over a wider range of possible orbits.

The results for the velocity error are shown in Figure 6 and Figure 7 for the vertical and horizontal network respectively. Please note, that the colorbar (range of error values coded in color) is stronger limited compared to the results for the 1 km network. This is done to show the distribution of error in regions where the error is small. The outliers at low orbit heights, where the error is rather large, are hereby aggregated with the same (yellowish) color. It can be seen that the overall behavior of the velocity error is quite similar to the location. With a general preference of the vertical network and vertical FoV and the *valley of low error*.

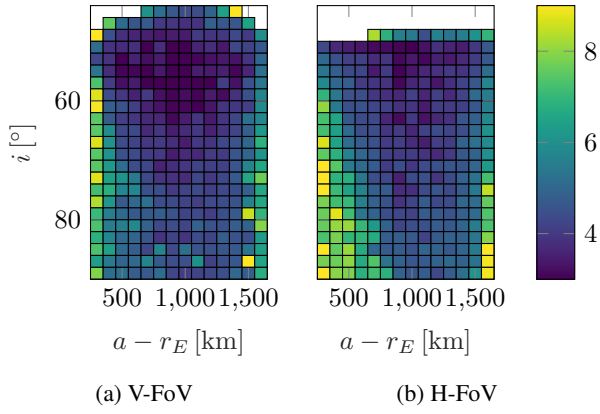


Figure 5: H-Net 500 km baseline error location Grid

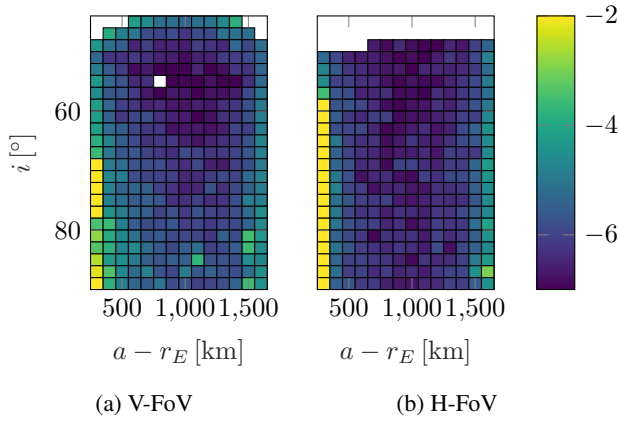


Figure 6: V-Net 500 km baseline error velocity Grid

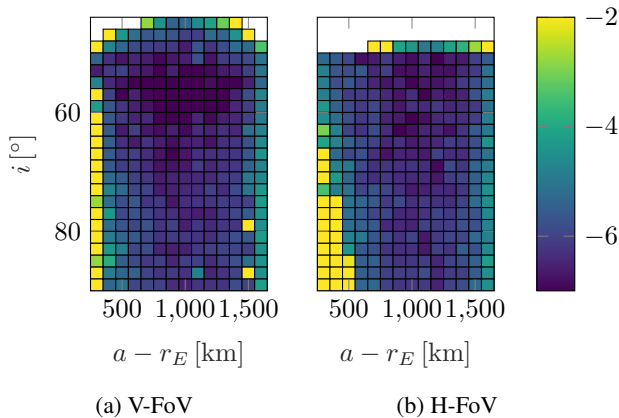


Figure 7: H-Net 500 km baseline error velocity Grid

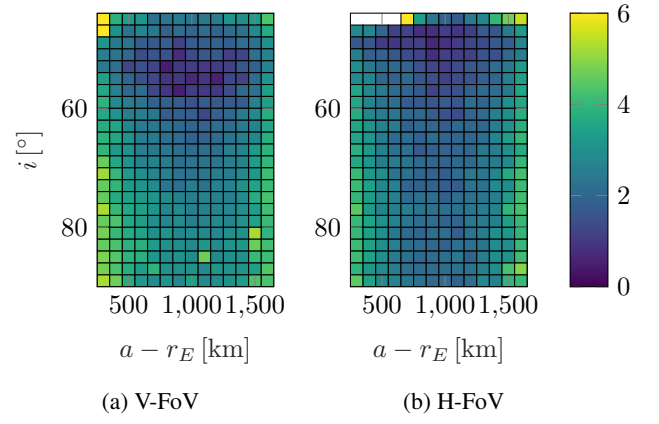


Figure 8: V-Net optimal error location Grid

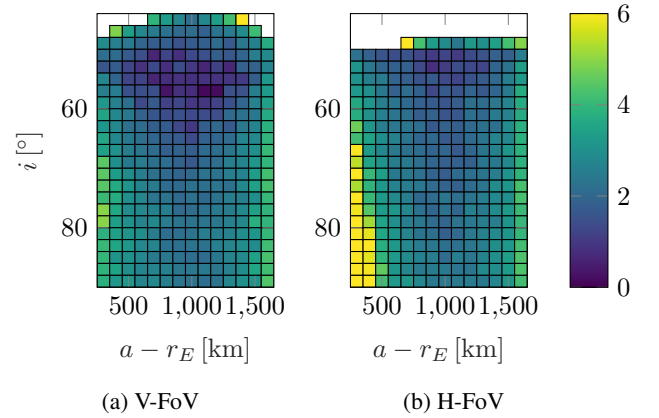


Figure 9: H-Net optimal error location Grid

### 3.3. Results Optimal Error

After analyzing the results for the two distinct network configurations using 1 km and 500 km separation, the question arises if there is a specific baseline that is to be preferred in all cases. The conclusion in [9] already indicated that this is not the case. From a theoretical point of view it would also be surprising if there is a *one size fits all* solution regardless of particular orbital parameters. However, the investigations in [9] did not fully consider if there are optimal baselines for parts of the orbital parameters.

The results presented in this section, show the smallest possible error encountered for a given orbit. This means for each orbit (i.e. orbit height and inclination) the errors of all the 20 different baselines are compared and the smallest one is depicted. The plots are again split into location (Figure 8, Figure 9) and velocity (Figure 10, Figure 11) errors and the different network types. Please note that the colorbar is modified, compared to the results of the 1 km and 500 km networks to make the plots easier to read. One of the purposes of investigating the smallest possible error is to assess how much off the error value for a particular baseline is from the optimum. For example, can 500 km be chosen as the baseline of choice? Is the

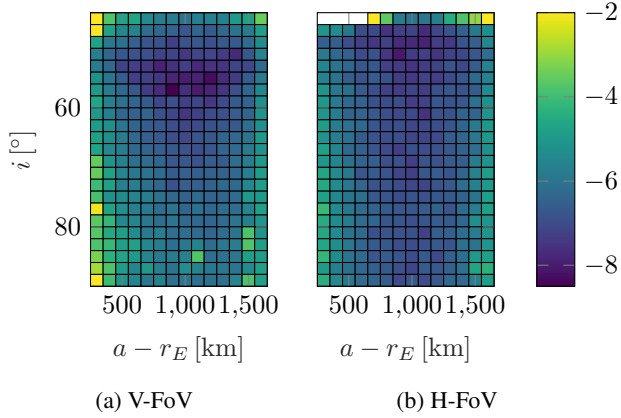


Figure 10: V-Net optimal error velocity Grid

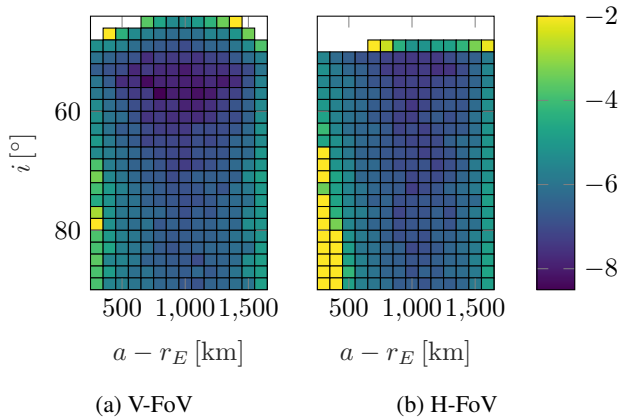


Figure 11: H-Net optimal error velocity Grid

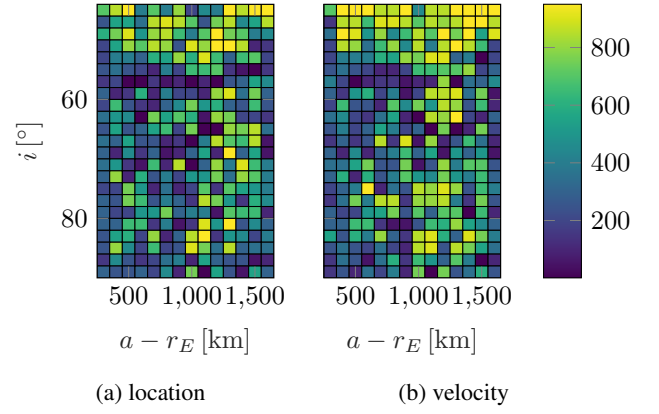


Figure 12: V-Net V-FoV optimal baseline

error at that baseline close to the smallest possible error or would too much potential be given away?

From the locations errors (Figure 8, Figure 9), it can be seen that the smallest possible error volume can be as low as  $1 \text{ m}^3$ . The largest minimum error volume apparently does not exceed an equivalent cube length of 100 m, except for the low orbits in the horizontal network with horizontal FoV. Please be reminded again that the error volume and therefore equivalent cube length do not distinguish skewed error ellipsoids. In general the range of errors (min vs max) is thus reduced compared to the results of a single baseline.

What is striking in the results is that the *valley of low error* is also present. Note, when the baseline is increased, the center of the network stays at a fixed latitude but both the transceiver and second receiver nodes are moving. Therefore, it is not clear if the location of the *valley of low error* at around  $50^\circ$  inclination is a feature of the orbits alone or a result of the relation between location of the center of the network and a particular inclination (range). The existence of the valley can be an indication that the accuracy of the determination of some orbits is fundamentally limited, no matter the choice of network. It is the expectation of the authors, that it might be possible to shift the location of the valley, by altering the orientation of the FoV and position of the center of the network, but it won't be possible to make it disappear entirely.

### 3.4. Results Optimal Baseline

The baseline at which the minimal error volume occurs is presented in this section. The arrangement of plots is altered, to show the results for location together with velocity for different network and FoV configurations. This is done, since ultimately a chosen baseline should be applicable to provide optimal error volumes in both location and velocity. The colorbar in the plots indicates the baseline in km.

Similar to the results presented in [9], there appears to be no clear indication for a single best baseline. For

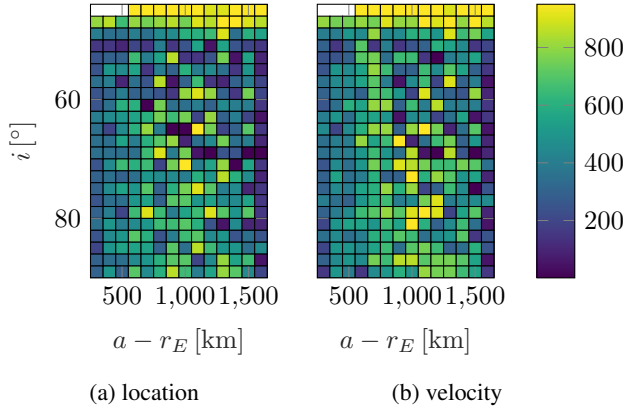


Figure 13: V-Net H-FoV optimal baseline

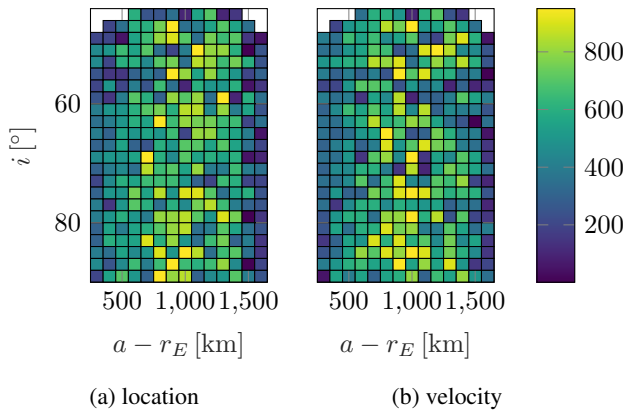


Figure 14: H-Net V-FoV optimal baseline

the vertical networks, shown in Figure 12 and Figure 13, there appears, however, to be a preference for larger baselines towards the lower inclinations and possibly higher to mid-range orbit heights.

For the horizontal networks, Figure 14 and Figure 15 indicate a preference for larger baselines only for the mid-range orbits and in general less dependency on the inclination. There appears to be little difference between the results regarding the location and velocity error.

Unfortunately, the results presented so far do not provide an indication as to how much the error varies if a suboptimal baseline is chosen. For example, consider a vertical network with vertical FoV (Figure 12). A shorter baseline of say 200 km is chosen, since shorter baselines tend to be preferable for lower orbits and higher inclinations. It is not possible to determine from the plots alone how close the error at 200 km is to the optimal baseline. Further work is needed to evaluate the evolution of the error volume along the baseline lengths and inspect if it is somehow proportional to the baseline length at all.

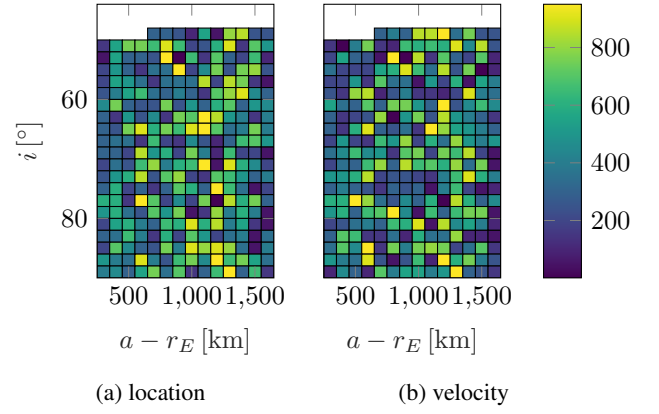


Figure 15: H-Net H-FoV optimal baseline

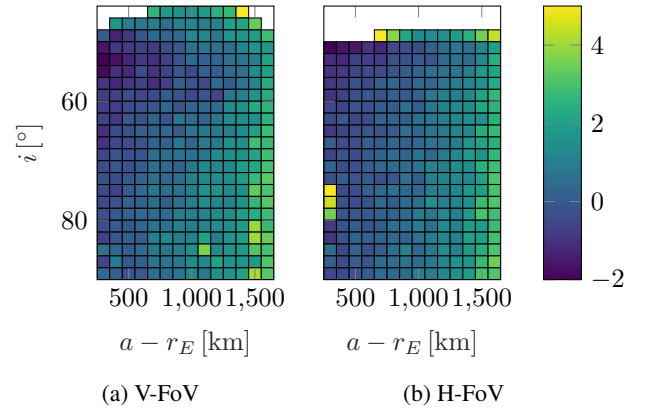


Figure 16: H-Net 1 km error location high resolution

### 3.5. Results High Resolution Processing

As mentioned in subsection 2.2 there are two random processes that influence the generation of observations for the simulations. The first characterizes the inherent randomness of estimated parameters due to measurement noise (i.e. finite SNR), while the second emulates the effect of a grid based processing procedure with limited step size. The step size chosen for the simulation is such that it dominates the variance of the generated parameters already at rather low SNR values. If a virtually grid-free estimator is used (such as gradient based nonlinear maximum likelihood estimators) a much lower variance can be achieved that reaches the theoretical limit imposed by the CRLB.

The plots in Figure 16 show the results for the location error of a network with 1 km baseline similar to subsection 3.1. The results for the velocity error are not shown as they provide the same conclusions. However, all values for  $\sigma_p$  are set to zero and thus disabling the impact of a processing grid. The values of the error volumes are overall much smaller compared to the grid case. Furthermore, the larger errors for low orbit heights disappeared and there is a general trend of increasing error with increasing orbit height noticeable. This trend could be explained with the decreasing SNR as the orbit heights in-

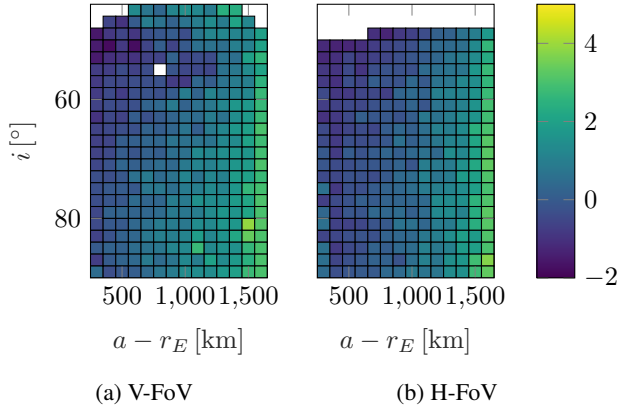


Figure 17: V-Net 500 km error location high resolution

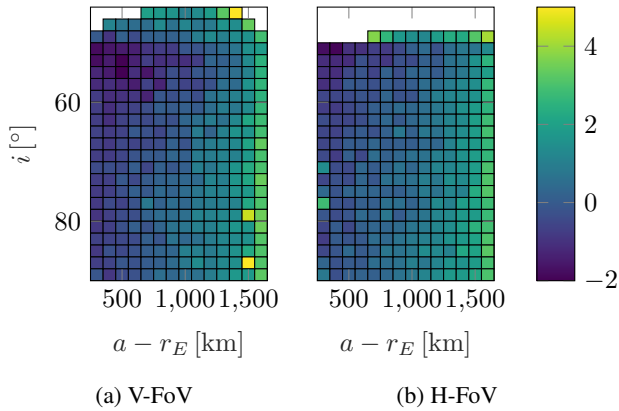


Figure 18: H-Net 500 km error location high resolution

crease and thus the CRLB also increases. The *valley of low error* is, if at all present, only weakly visible. In general it appears that the high accuracy of the estimated parameters compensates for any geometrical effects. This is also supported by the results for 500 km baseline shown for the location error in Figure 17 for the vertical and in Figure 18 the horizontal network respectively.

The outcomes for the minimal error volume are omitted as they show the same tendency. This means that the trend of higher errors is towards higher orbits (presumably due to the decreasing SNR) and less variation with respect to the inclination. Regarding the resulting baseline of minimal error the conclusions are similar to the grid based processing in that no clear favorite can be determined. If anything, the best baselines may be slightly smaller, probably caused by higher baselines yielding higher ranges to the targets and thus smaller SNRs.

It must be noted that the case of high resolution processing as assumed in the simulations is most probably only of theoretical value. Due to the high achievable SNRs, the CRLB is typically very low. This results in highly accurate estimates for especially the range. The estimates can be as close as a few wavelengths to the ground truth. While this is perfectly normal in theory, it is highly questionable if the assumption of a single target

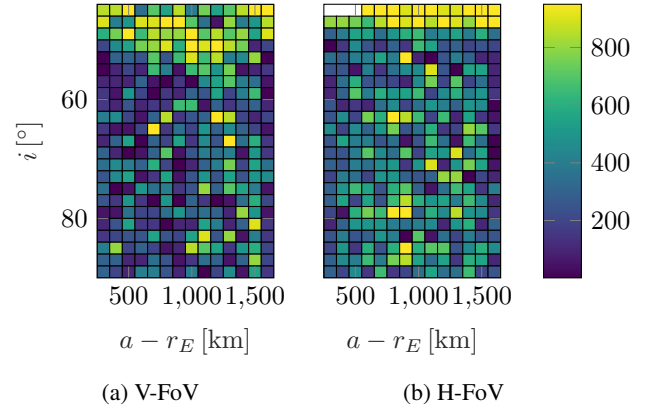


Figure 19: V-Net optimal error baseline high resolution

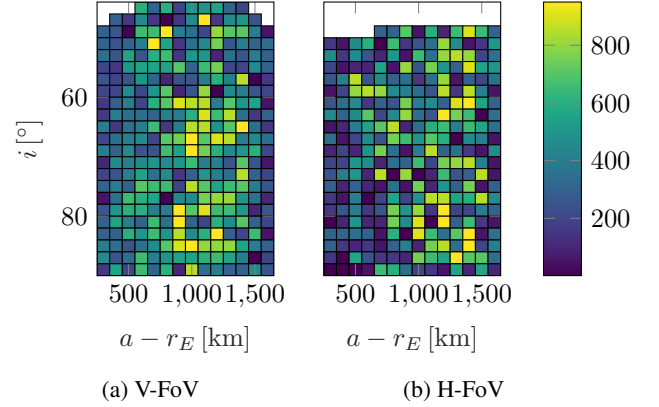


Figure 20: H-Net optimal error baseline high resolution

with a single reflecting point is valid in practice. Targets with RCSs large enough to create high SNRs are most probably extended, with multiple scattering or reflections points. Thus, the signal received from the target is not that of a single one anymore but the superposition of many reflections requiring in general a multitarget estimation framework. While such frameworks exist (super-resolution techniques do in fact rely on jointly estimating multiple signals), they were not employed in the simulations at hand. Furthermore, super-resolution requires accurate knowledge about the behavior of the radar, in terms of frequency response, waveform of the transmit signal and calibration of the antennas used. Such knowledge is not necessarily available for all types of radar systems. Nonetheless, the investigations conducted here allow to assess what is theoretically possible.

#### 4. CONCLUSION

The aim of this paper is to present a simulation framework to assess the capabilities of a network of two radars to detect objects in space on a Keplerian orbit and determine their orbital parameters. The work is extending [9] by evaluating networks with both horizontal and vertical oriented baselines in conjunction with different orienta-

tions of the FoV. Observations from the radar nodes are simulated using objects in Keplerian orbits and random processes. The randomness is caused by inevitable measurement noise and possible quantization effects when a grid based signal processing scheme is used. The accuracy of orbit determination is verified using the PCRLB of a tracking based approach. A major conclusion is the presence of a *valley of low error* which denotes a range of orbit inclinations and heights where the error, both for a specific baseline and the minimal error over all baselines, is lowest. It is yet to be determined how this correlates with the location of the center of the network and the direction of the center of the FoV. As expected, a single best baseline for all orbits could not be found. However, a different distribution of optimal baselines between a horizontally or vertically aligned network was found. If the range of orbits is further restricted (i.e. smaller range of inclination and heights) it is possible that a best baseline can be identified. It is unlikely that there is just one network configuration that fits to all orbits. The impact of a grid based signal processing scheme was also analyzed. When the accuracy of estimated observation parameters is limited by the grid size, instead of the CRLB, the choice of the network layout appears to have a stronger impact on the determined orbital parameters. In the future further investigations should be performed to assess how feasible high resolution methods are for space surveillance radars and if they truly lead to performances less depending on the network geometry (and potentially more on the sheer number of nodes).

## ACKNOWLEDGMENTS

The work presented in this paper was funded by the German Federal Ministry for Economic Affairs and Climate Action under the funding code 50 LZ 2005. Responsibility for the content of this publication lies with the author.

## REFERENCES

1. T. Schildknecht. Optical surveys for space debris. *The Astronomy and Astrophysics Review*, 14(1):41–111, Jan 2007. ISSN 1432-0754. doi: 10.1007/s00159-006-0003-9. URL <https://doi.org/10.1007/s00159-006-0003-9>.
2. M. A. Steindorfer, G. Kirchner, F. Koidl, P. Wang, and D. Kucharski. Space debris science at the satellite laser ranging station graz. In *2017 IEEE International Conference on Environment and Electrical Engineering and 2017 IEEE Industrial and Commercial Power Systems Europe (EEEIC/I CPS Europe)*, pages 1–5, June 2017. doi: 10.1109/EEEIC.2017.7977641.
3. J. Klare, F. Behner, C. Carloni, D. Cerutti-Maori, L. Fuhrmann, C. Hoppenau, V. Karamanavis, M. Laubach, A. Marek, R. Perkuhn, S. Reuter, and F. Rosebrock. The future of radar space observation in europe—major upgrade of the tracking and imaging radar (tira). *Remote Sensing*, 16(22), 2024. ISSN 2072-4292. doi: 10.3390/rs16224197. URL <https://www.mdpi.com/2072-4292/16/22/4197>.
4. M. Albrecht, D. Behrendt, M. Gilles, M. Käske, C. Knauf, P. Müller, L. Prünte, and C. Reising. Improvements of gestra – a phased-array radar network for the surveillance of resident space objects in low-earth orbit. In *2nd NEO and Debris Detection Conference*, volume 2, 2023.
5. N. Neuberger, S. Kollecker, M. Käske, S. Horstmann, and L. Prünte. Gestra: First results of leo objects detection and parameters estimation. In *2nd NEO and Debris Detection Conference*, volume 2, 2023.
6. Victor S Chernyak. *Fundamentals of multisite radar systems: multistatic radars and multistatic radar systems*. CRC Press, 1998.
7. J. Vierinen, J. Markkanen, H. Krag, J. Siminski, and A. Mancas. Use of EISCAT 3d for observations of space debris. In T. Flohrer and F. Schmitz, editors, *Proc. 7th European Conference on Space Debris*, Darmstadt, Germany, 18–21 April 2017. Vierinen, JuhaMarkkanen, JussiKrag, HolgerSiminski, JanMancas, Alexandru, ESA Space Debris Office. URL <https://conference.sdo.esoc.esa.int/proceedings/sdc7/paper/350>.
8. Th Michal, JP Eglizeaud, and J Bouchard. GRAVES: the new french system for space surveillance. In *4th European Conference on Space Debris*, volume 587, pages 61–66, 2005.
9. C. Knauf, R. Hoffmann, H. Schily, A. Charlish, M. Gonzalez, and R. Kohlleppe. Performance analysis of a two node radar network geometry on orbit estimation accuracy. In *8th European Conference on Space Debris*, volume 8, 2021.
10. D. Vallado. *Fundamentals of Astrodynamics and Applications*. Microcosm Press, 4th edition, 2013.
11. M. Richards, J. Scheer, and A. William. *Principles of Modern Radar: Basic principles*. The Institution of Engineering and Technology, 2010. doi: 10.1049/SBRA021E. URL <https://digital-library.theiet.org/doi/abs/10.1049/SBRA021E>.
12. S. Kay. *Fundamentals of Statistical Processing, Volume I: Estimation Theory*. PRENTICE HALL, 1993.
13. D. Barton. *Radar system analysis and modeling*. Artech House, 2004.
14. H. Van Trees and K. Bell. *Bayesian Bounds for Parameter Estimation and Nonlinear Filtering/Tracking*. Wiley-IEEE Press, 2007.